Permittivity Estimation Using Coupling of Commercial Ground Penetrating Radars

Greg Hislop, *Senior Member, IEEE*

***Abstract*—A novel method is presented for the characterization of dielectric grounds. The technique measures frequency shifts in a radar's crosstalk and links them to ground permittivity. The method is simple to implement and operates in real time. It may be implemented on the early-time signal of any ground-coupled radar and requires no knowledge of the system's antennas or feed structure. Accurate permittivity measurements are obtained, which may be then used to obtain depth estimates or as an input to inverse scattering and imaging techniques.**

***Index Terms*—Antennas, geophysical measurement techniques, geophysical signal processing, ground penetrating radar, permittivity, radar measurements, radar theory, radar remote sensing, soil moisture, soil properties, ultra wideband radar.**

I. Introduction

GROUND penetrating radar (GPR) has many applications, including road surface investigation [1]–[4], land mine detection [5]–[11], tree trunk imaging [12], [13], mining [14]–[16], the nondestructive testing of concrete structures [1], [4], [17], [18], through/in-wall imaging [19], [20], and the exploration of planetary bodies [21], [22]. For all of these applications, it is important to have or to be able to measure the permittivity of the medium under investigation. Knowing this value in turn gives one the wave velocity in the medium. This is regularly required for depth estimation [16], [23], inverse scattering [5], [8], [21], and source localization purposes [5], [23], [24]. There are numerous existing methods of estimating the permittivity/wave velocity.

A common midpoint method takes measurements with a range of transmitter-to-receiver offsets and assumes that a reflector is present in the ground in line with the midpoint between the antennas. A set of simultaneous equations involving baseline lengths and propagation times then allows one to solve for the permittivity. The disadvantage is that the technique is either labor intensive or requires a large array. In addition, it is assumed that the permittivity is laterally constant and that a suitable buried reflector is present [25], [26]. A second technique involves the presence of a buried point scatterer that will give a hyperbolic radar return (in a B-scan or the propagation time versus the radar position in space). Characterizing the shape of this hyperbola allows one to obtain the permittivity. The disadvantage is the need for a buried object to be both present and known to be a point scatter in nature [27], [28]. A third approach, which is similar to the previous approach, involves using inverse scattering algorithms with a range of prospective permittivity values in order to find the permittivity that best reconstructs the scatterer. This has the disadvantage of requiring significant computation time and the presence of a known scatterer [29]. A fourth set of techniques uses complicated and often full-wave (e.g., the method of moments or the finite-difference time domain) methods of simulating radars on top of dielectric grounds and coupling these with iterative optimization techniques to find the permittivity that matches the simulations to measurements. These techniques have the disadvantage of requiring significant computational resources and being complicated to implement [30]–[33]. In the fifth approach, one may take the more direct approach of designing probes that penetrate the soil or extracting soil samples and using standard laboratory permittivity measurements [34]. In recent time, some authors have turned their attention to the crosstalk between a transmitter and a receiver (or early-time signal features) of ground-coupled bistatic radars with small to negligible antenna spacing. In these works, the magnitude of the crosstalk (or the envelope thereof) is used as a measure of ground permittivity [13], [35]–[39]. Frequency shifts in the crosstalk due to the ground's presence were briefly introduced for permittivity estimation in [40], and this paper vastly expands on this work.

It is well known that immersing an antenna in a dielectric decreases the frequency at which it achieves optimum radiating efficiency. This is often used to decrease the antenna size while maintaining low operating frequencies. The effect of dielectric loading is also present for antennas that are in air but in contact with a dielectric surface. This paper proposes a model that links the frequency shift of any arbitrary ground-coupled radar to the permittivity of the ground. A calibration procedure is also proposed. The result is a technique that accurately measures the ground permittivity using any on-ground radar. No knowledge of the radar used is required, thus allowing application to commercial radars. Both the measurement method and the calibration process are simple to understand and fast to operate. The technique works on grounds of any conductivity that allows for even small penetration.

This paper starts by explaining the permittivity estimation procedure in Section II. Section III-A then validates the technique using the simulations of several common GPR types before Section III-B presents a software model of a commercial GPR (the SIRO-Pulse) and demonstrates that the technique works on these data. In Section IV, the technique is verified using the experimental measurements of three different commercial radars, including the SIRO-Pulse and the Geophysical Survey Systems Inc., (GSSI) 1.6- and 2.6-GHz units. A discussion follows in Section V before Section VI concludes this paper.

Manuscript received August 14, 2014; revised November 17, 2014; accepted December 30, 2014.

The author is with Energy Flagship, Commonwealth Scientific and Industrial Research Organisation, Brisbane, QLD 4069 Australia (e-mail: greg.hislop@csiro.au).

Digital Object Identifier 10.1109/TGRS.2015.2392110

II. Permittivity Estimation Procedure

Consider a nonmagnetic ($\mu = \mu_0$) nondispersive homogeneous medium of permittivity $\varepsilon = \varepsilon_0(\varepsilon_r' - j\varepsilon_r'')$ and loss tangent $T = \varepsilon_r''/\varepsilon_r'$ ($T \ll 1$, i.e., only low-loss materials are considered). The wavelength within said medium may be expressed in terms of frequency f and the material permittivity as

$$\lambda = \frac{1}{f\sqrt{\mu_0\varepsilon_0\varepsilon_r'}}. \tag{1}$$

Any given antenna inside the medium in question will possess a wavelength, i.e., λ_e, at which it has maximum radiation efficiency (e.g., $\lambda_e = 2L$ for an L-length dipole). If ε_r' is increased in (1), the frequency f_e that corresponds to λ_e and thus at which maximum efficiency occurs decreases. This is known as dielectric loading and is often used to reduce the antenna size while maintaining low-frequency operation. If λ_e is known for a given antenna, measuring f_e will then allow one to estimate the ε_r' of the medium in which the antenna is placed via

$$\varepsilon_r' = \frac{1}{f_e^2\lambda_e^2\varepsilon_0\mu_0}. \tag{2}$$

Consider a planar antenna directly placed on (or with a slight offset due to the antenna's substrate or plastic protective cover) an air/earth interface. In this case, f_e is affected by both mediums. The portions of the near field in the earth encourage the inverse square relationship between ε_r' and f_e in (2). However, as the medium permittivity is known, the fields in air encourage a fixed value of

$$\varepsilon_r' = \frac{1}{f_e^2\lambda_e^2\varepsilon_0\mu_0} = 1. \tag{3}$$

Thus, there are two dominant effects on the ε_r' and f_e relationship, i.e., one constant and one square in nature. In addition, there are no effects expected to introduce a higher order relationship. With this in mind, the author proposes the following quadratic relationship between the earth's permittivity ε_r' and the antenna's optimal frequency f_e:

$$\varepsilon_r' = \frac{a}{f_e^2} + \frac{b}{f_e} + c \tag{4}$$

where a, b, and c are the system-dependent model parameters to be calculated. These values may be obtained by measuring the radar in question's f_e in air and on two or more mediums of prior known ε_r'. Three or more simultaneous equations are then obtained via (4), allowing for the calculation of the model parameters. In the cases presented in this paper, the calibration procedure is performed on one air measurement and two measurements on grounds of known permittivity. The proposed permittivity estimation procedure may be summarized as follows.

1) For the calibration, place the radar on three or more flat mediums of known permittivity (one may be air).
2) Collect an A-scan (a single GPR measurement, see Fig. 1) for each of these mediums, and isolate the transmitter-to-receiver crosstalk via temporal truncation.
3) Use the Fourier transform to obtain the magnitude of the crosstalk as a function of frequency, and locate signal maximum f_m (see Fig. 2).

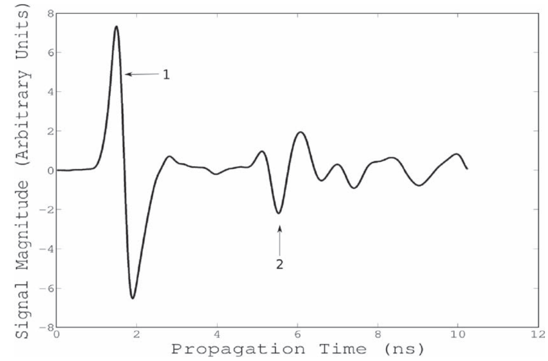

Fig. 1. A-scan collected using a GSSI 2.6-GHz radar on wet sand in a plastic tub. 1: transmitter-to-receiver crosstalk; 2: return from the bottom of the tub.

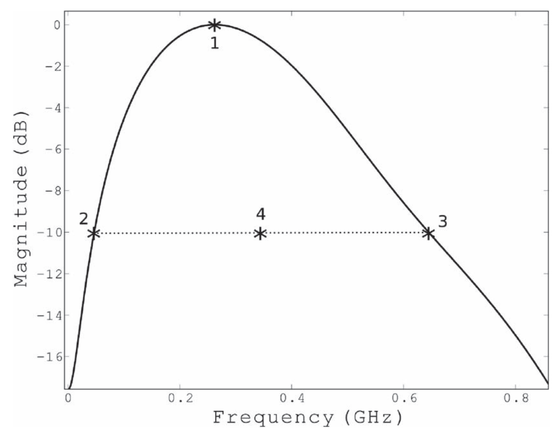

Fig. 2. Normalized magnitude of the Fourier transform of the crosstalk component of the A-scan in Fig. 1. 1: maximum at f_m; 2: low-frequency −10-dB point f_{low}; 3: high-frequency −10-dB point f_{high}; 4: center of the frequency range f_e.

4) Find the frequencies (f_{low} and f_{high}) on either side of the maximum frequency response at which the response drops by X dB ($X = 10$ in this paper).
5) Record $f_e = (f_{\mathrm{low}} + f_{\mathrm{high}})/2$ for each calibration material.
6) Find the model parameters a, b, and c that provide a least squares match of the calibration f_e and ε_r' values to (4).
7) Place the radar on a flat surface of unknown material, and calculate f_e as per the aforementioned procedure.
8) Use (4) to estimate ε_r'.
9) Repeat 7 and 8 for each unknown material.

It should be noted that one could use the frequency of maximum return f_m as optimal frequency f_e. However, ultrawideband instruments have an f_m that is unstable in the presence of noise. Band cutoffs f_{low} and f_{high} present more stable values, and as such, the author uses the center of the X dB band as f_e.

The following sections will now test this theory first on simulated data and then using three different commercial GPR units.

III. Simulated Results

A. Verification With Elementary GPR

To the author's knowledge, no analytical solution exists to the problem of a physically realizable antenna on a dielectric interface. For this reason, an intuitive approach has been used to introduce the proposed quadratic relationship between ε_r

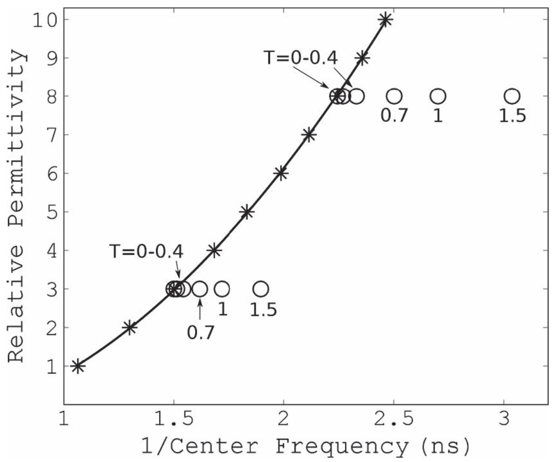

Fig. 3. (Stars) Ground ε_r' versus the inverse of the 10-dB band center frequency (f_e) obtained via the simulation of a 15-cm-long dipole. (Solid line) Least squares fit to the quadratic model. (Circles) Constant permittivity of 3 and 8, with losses of $T = [0,\ 0.025,\ 0.05,\ 0.075,\ 0.1,\ 0.15,\ 0.25,\ 0.4,\ 0.7,\ 1,\ 1.5]$.

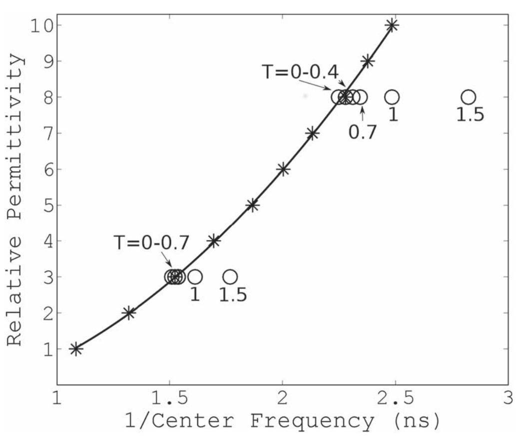

Fig. 4. (Stars) Ground ε_r' versus the inverse of the 10-dB band center frequency (f_e) obtained via the simulation of a 15-cm-long dipole pair that is 7.5 cm apart. (Solid line) Least squares fit to the quadratic model. (Circles) Constant permittivity of 3 and 8, with losses of $T = [0,\ 0.025,\ 0.05,\ 0.075,\ 0.1,\ 0.15,\ 0.25,\ 0.4,\ 0.7,\ 1,\ 1.5]$.

and f_e. It is difficult to prove the model's validity for all ground-coupled GPRs. Thus, this section will use a method of moments solution to Maxwell's equations in a surface integral form with a layered-media Green's function (via the FEKO software suite) to verify the model for three common GPR types. These are full-wave simulations and thus provide an exact solution (within machine precision) for the given antenna mesh and ground parameters. The scattering matrix parameters have been simulated across frequency for a single dipole, a dipole pair, and a bowtie pair. Figs. 3–5 plot the relationship between the permittivity and f_e, and they show a quasi-exact match to quadratic model (4) in each case. A large range of loss tangent T values at $\varepsilon_r = 3, 8$ is tested and shows that the model holds for all but very large losses. Section IV will demonstrate that large losses of $T \geq 0.3$ lead to negligible ground penetration and thus are not of concern. The author has also obtained comparable results for dipoles/bowties with a range of antenna separations, operating bands, and resistively

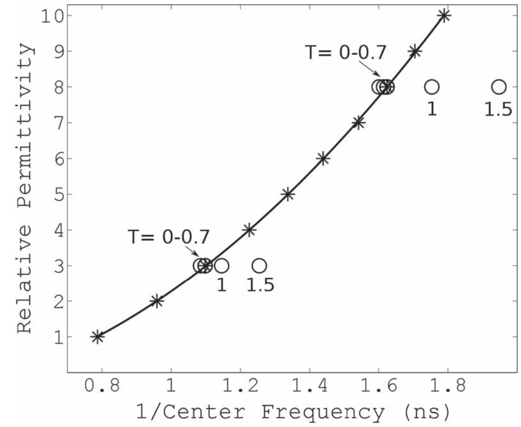

Fig. 5. (Stars) Ground ε_r' versus the inverse of the 10-dB band center frequency (f_e) obtained via the simulation of a pair of bowtie antennas separated by 4.5 cm, consisting of triangles that are 2.5 cm high with a 66.8° flare angle. (Solid line) Least squares fit to the quadratic model. (Circles) Constant permittivity of 3 and 8, with losses of $T = [0,\ 0.025,\ 0.05,\ 0.075,\ 0.1,\ 0.15,\ 0.25,\ 0.4,\ 0.7,\ 1,\ 1.5]$.

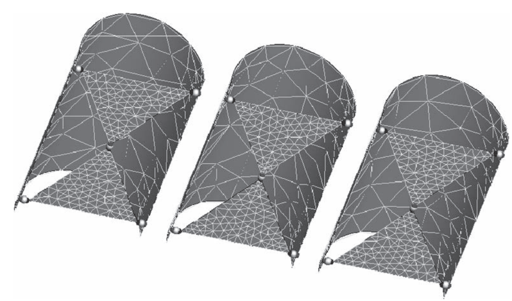

Fig. 6. FEKO model of the SIRO-Pulse radar. Note that the layered-media Green's functions were used to represent the antenna substrate, the plastic casing, and the earth material, none of which are shown.

loaded shields (results not shown). The remainder of this paper shall now test the theory on commercial instruments.

B. Simulation of Commercial Radar

One of the commercial systems to be considered in this paper is the 800-MHz SIRO-Pulse, i.e., an impulse GPR unit produced by the Commonwealth Scientific and Industrial Research Organisation in Australia. As the unit casing is easily opened, the author was able to measure a number of important antenna parameters and thus perform simulations of the radar using the FEKO electromagnetic simulation software. The unit is pictured in Fig. 6 and consists of three bowtie antennas that are resistively loaded to their respective shielding plates. The center element is the transmitter, and the outer elements are the receivers. The presence of the two receivers allows for crosstalk and ground surface removal by the radio-frequency subtraction of the two received signals. As the crosstalk is of utmost importance to the permittivity estimation technique in question, only the signal received at one of the receivers is used throughout this paper. Visual inspection and permittivity measurement via a coaxial probe allowed the simulation to incorporate the antenna and shield dimensions, the value of resistive loading, and the permittivity and thickness of the antenna substrate and the plastic protective casing. However,

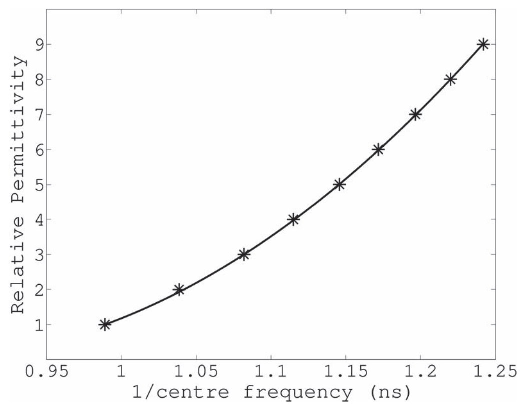

Fig. 7. (Stars) Ground ε_r' versus the inverse of the 10-dB band center frequency (f_e) obtained via simulation. (Solid line) Model obtained using $\varepsilon_r' = 1, 3$, and 8 as calibration points.

as no information could be obtained on the transmitted pulse shape or the baluns, the simulations considered the transmitter to be excited by a frequency-constant unit voltage across the two closest points of the bowtie halves, whereas the received signal was measured across the equivalent points on one of the receivers, and the other was terminated in a load. The antenna substrate, the plastic protective casing, and the underlying earth were simulated using planarly layered Green's functions.

The radar was simulated in air and then lying on eight different soil types with permittivity values of 2, 3, 4, 5, 6, 7, 8, and 9, each with a moderate loss tangent of $T = 0.1$. The model in (4) was applied using the three cases of $\varepsilon_r' = 1, 3$, and 8, (i.e., air with two known grounds) as the calibration measurements. The obtained quadratic was (note that f_e is in units of GHz)

$$\varepsilon_r' = \frac{64}{f_e^2} - \frac{110}{f_e} + 48. \tag{5}$$

Equation (5) and the ten simulations are plotted in Fig. 7, which clearly validates the proposed model. The author's main interest in estimating the ground permittivity is in obtaining the exact depth d to buried reflectors. As the medium wave velocity is $1/\sqrt{\mu_0\varepsilon_0\varepsilon_r'}$, the percent error in the depth estimate due to ε_r' being incorrectly estimated as $\tilde{\varepsilon}_r'$ is

$$\Delta d = 100 \left| \sqrt{\frac{\tilde{\varepsilon}_r'}{\varepsilon_r'}} - 1 \right|. \tag{6}$$

Equation (6) is calculated in Fig. 8 for the ten different soil permittivity values simulated. An acceptably small error is obtained (note that the error is 0 at the calibration points). To investigate the effect of material loss on the proposed algorithm, the radar was simulated at $\varepsilon_r' = 3, 8$ with a range of loss tangents varying from $T = 0$ to $T = 1.5$. The resulting errors are presented in Figs. 9 and 10 as a function of the loss tangent. In both cases, the error is below 7% for all loss tangents below $T = 0.3$. It should be noted that, for a T of 0.3 or above, the material loss is large, leading to limited or no ground penetration; as such, high-loss scenarios are of limited interest.

This section has verified the proposed algorithm against simulated data. The following section shall verify that the technique works on the experimental data by applying the technique to three different commercial radars.

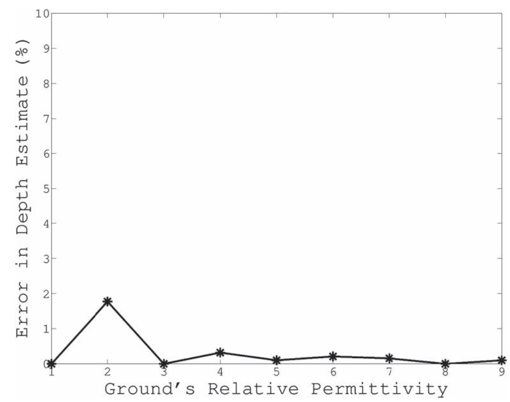

Fig. 8. Percent error in the reflector depth estimation due to errors in the ε_r' estimation versus the actual ε_r': the case of SIRO-Pulse simulations.

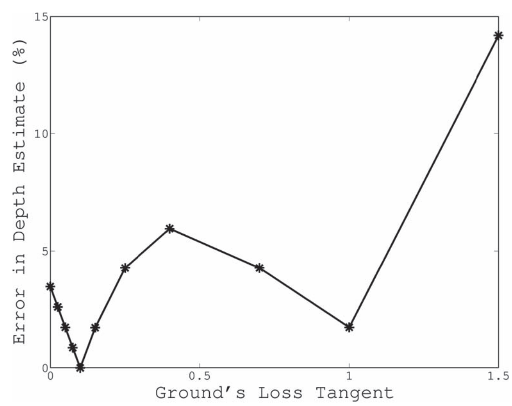

Fig. 9. Percent error in the reflector depth estimation versus loss tangent T: the case of SIRO-Pulse simulations $\varepsilon_r' = 3$.

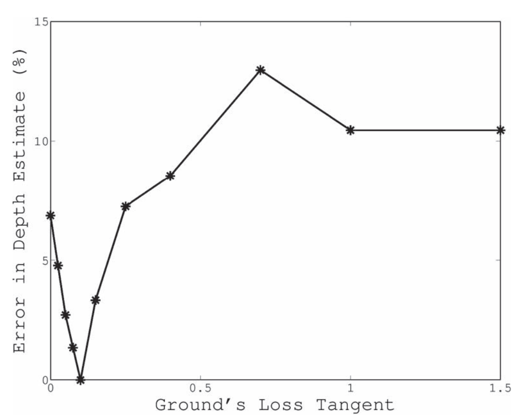

Fig. 10. Percent error in the reflector depth estimation versus the ground's loss tangent T: the case of SIRO-Pulse simulations $\varepsilon_r' = 8$.

IV. Experimental Results With Commercial GPR

A. SIRO-Pulse

The first commercial radar considered for experimental measurements was the 800-MHz SIRO-Pulse instrument. To perform these tests, a metal plate was placed in the bottom of a 41-L plastic container that was then filled with various materials to be tested. The surface was leveled by running a straight-edged piece of timber over it. The antenna was then placed on the material in question, and an A-scan collected.

This was done with the plate at two different depths $d_1 = 15.5$ cm and $d_2 = 10.5$ cm. The use of multiple depths facilitates an accurate measurement for the ground-truth permittivity using the measurement of the propagation time from the transmitter to the metal plate to the receiver. The advantage is that the time of signal emission t_0 and the velocity of propagation along the surface between the transmitter and the receiver need not be calculated. If $t_{1,2}$ is the time that the metal plate's reflection is received, for the two depths measured and with x being the transmitter-to-receiver offset, then the total propagation time from the transmitter to the plate to the receiver is

$$t_{1,2} = \sqrt{\varepsilon_r' \varepsilon_0 \mu_0 \left(x^2 + 4d_{1,2}^2\right)}. \tag{7}$$

Subtracting (7) for subscript 2 from that of subscript 1 and rearranging gives a reliable ground-truth value for the permittivity as

$$\varepsilon_r' = \frac{(t_1 - t_2)^2}{\mu_0 \varepsilon_0 \left(\sqrt{x^2 + 4d_1^2} - \sqrt{x^2 + 4d_2^2}\right)}. \tag{8}$$

An f_e value was obtained from each material by considering the time-gated crosstalk signal component of the A-scan from the d_1 case. Only the direct transmitter-to-receiver coupling was considered, with the metal plate reflection removed via time gating.

To obtain a range of ground permittivity values, dry sand was initially used. Demineralized water was then added in 15 even stages, allowing for tests with 16 different mixtures ranging from 0% to approximately 14% water content by mass. Readers interested in soil moisture content estimation should note that, for all results in this paper, the ground-truth permittivity monotonically increased with respect to the water content and that, due to the experimental procedure used, stated moisture contents are approximate values only. A cement mixer was used to ensure a homogeneous mix, with the water content limited to 14% due to the sand sticking to the mixer sides, making for a nonhomogeneous mix. Other materials measured include air, wood, coal, clay garden pavers, a finer grained white sand, gravel, and dirt. The air and two of the wet sand measurements ($\varepsilon_r' = 2.3$ and 9.3, one mid range and the highest permittivity soil) were used as the calibration points. The resulting quadratic was

$$\varepsilon_r' = \frac{29.8}{f_e^2} - \frac{46.3}{f_e} + 18.5. \tag{9}$$

Fig. 11 plots the ground-truth ε_r' versus $1/f_e$ for each of the tested mediums. The calibrated model in (9) is present, as well as the model from the simulated results in the previous section. This plot clearly demonstrates the validity of the model against the experimental data. In addition, a close match has been obtained between the simulations and the measurements, with the differences likely to be due to the absence of knowledge of the baluns and transmitted pulse parameters. A slight rotation/lateral stretching of the quadratic for the simulated results would largely correct the remaining error. This suggests that the baluns/pulse shape may be together represented as a linear filter with a slight trough in the center of the frequency response. The percentage errors in the depth estimation that correspond to the variation from the calibrated model in (9) are plotted in Fig. 12. It can be seen that all of the materials in question were characterized within a reasonable level of accuracy (i.e., less than 10% error).

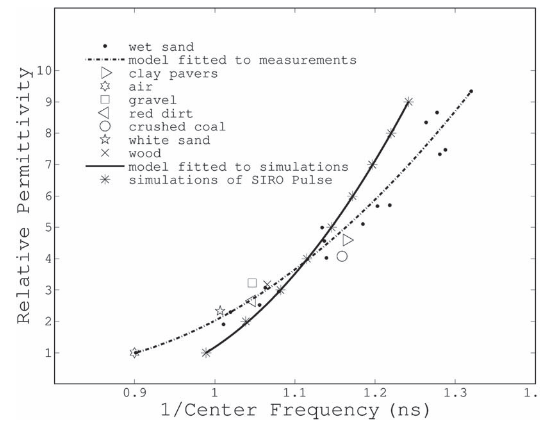

Fig. 11. Ground-truth soil ε_r' versus the inverse of the 10-dB band center frequency (f_e) obtained with the SIRO-Pulse measurements on top of various materials. (Broken line) Calibrated model. The simulations from Fig. 7 are included for comparison.

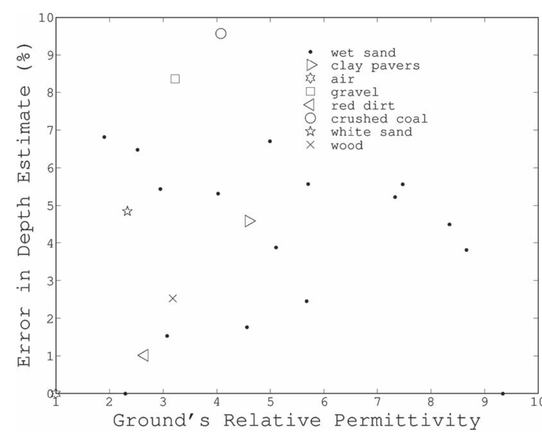

Fig. 12. Percent error in the reflector depth estimation versus the ground-truth soil permittivity: the case of SIRO-Pulse measurements.

B. GSSI Radars

Two radar units from GSSI were also tested. These were the 1.6- and 2.6-GHz units. In this case, the protective plastic casing could not be removed to study the antenna structure. As such, the simulation of the radar unit was not possible. Thus, the proposed model was applied with no knowledge of the unit's hardware. In this case, a smaller tub of 10-L volume and 10-cm depth was used. The tub was filled with each prospective ground material; the surface smoothed, and a single A-scan collected with each of the two radar units placed on top of the material under test. A sample of the material was then placed inside a calibrated WR770 waveguide connected to a network analyzer, and the permittivity and the loss tangent were accurately measured [41]. The method of obtaining the ground-truth material characterization needed to change from that used for the SIRO-Pulse as, in the case at hand, the transmitter-to-receiver baseline was not known and the measurement of the material loss was required.

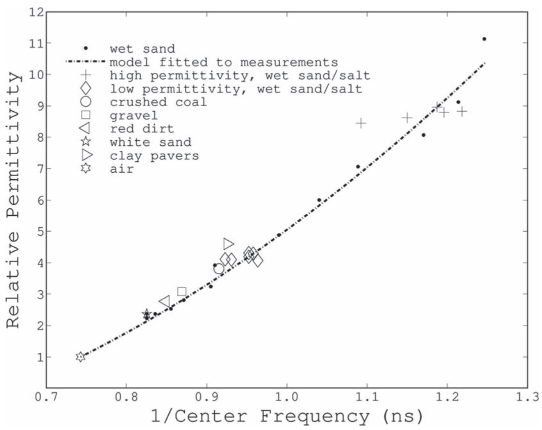

Fig. 13. Ground-truth soil ε_r' versus the inverse of the 10-dB band center frequency (f_e) obtained with the GSSI 1.6-GHz unit on top of various materials. (Broken line) Calibrated model.

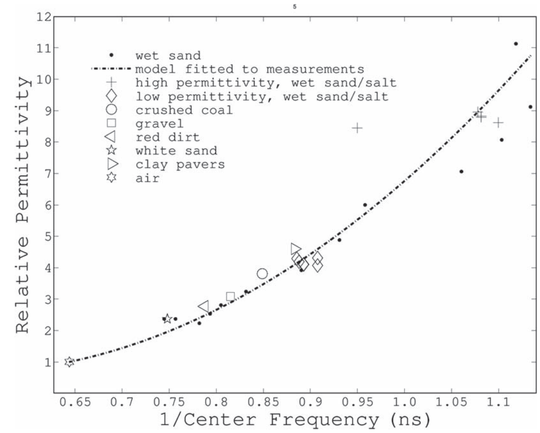

Fig. 14. Ground-truth soil ε_r' versus the inverse of the 10-dB band center frequency (f_e) obtained with the GSSI 2.6-GHz unit on top of various materials. (Broken line) Calibrated model.

As before, these tests were performed for a range of sand/water mixtures with a cement mixer used to obtain a homogeneous mix, obtaining ε_r' ranging from 2.2 to 11.1 with water contents ranging from 0% to approximately 20% by mass. In addition to this, two sets of tests were performed, where the material loss was controlled by starting with a fixed sand/water mixture and progressively adding salt. One of the sets of controlled loss tests had a near-constant ε_r' of around 4.2 (approximately 8% water), whereas the other set was stable around 8.7 (approximately 17%water). Finally, the measurements were also taken using dry finer white sand, coal, clay pavers, gravel, red dirt, and air. As the tub was considerably smaller than in the SIRO-Pulse case, only the initial positive half-cycle of the crosstalk (e.g., the first half of the crosstalk in Fig. 1) was used to obtain f_e, with the reflection from the bottom/sides of the tub having a small effect on the later half of the pulse (for low-permittivity soils). To calibrate the model to the two instruments, the air and the two initial (saltless) measurements in the two variable-loss tests were used as the calibration points.

The models (4) resulting from the calibration procedure were

$$\varepsilon_r' = \frac{11.5}{f_e^2} - \frac{4.2}{f_e} - 2.2 \tag{10}$$

for the 1.6-GHz unit and

$$\varepsilon_r' = \frac{27.8}{f_e^2} - \frac{29.5}{f_e} + 8.5 \tag{11}$$

for the 2.6-GHz unit. These calibrated models are plotted in Figs. 13 and 14, respectively, along with the points obtained using a wide range of test materials. These figures show that the proposed quadratic model gives an accurate estimation of the ground permittivity for a wide range of material types. The resulting percent error in the depth estimation using (6) for the GSSI 1.6- and 2.6-GHz units is plotted in Figs. 15 and 16, respectively. This is done for a range of materials as a function of each material's ground-truth permittivity value. These figures show that all but one of the measurements resulted in small errors of less than 10%. The one out riding result is wet sand with the largest tested salt content for the GSSI 2.6-GHz instrument. The loss tangent in this case was measured as

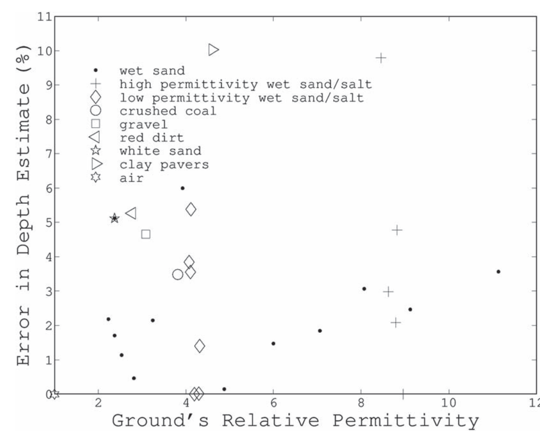

Fig. 15. Percent error in the reflector depth estimation versus the ground-truth soil permittivity: the case of the GSSI 1.6-GHz radar.

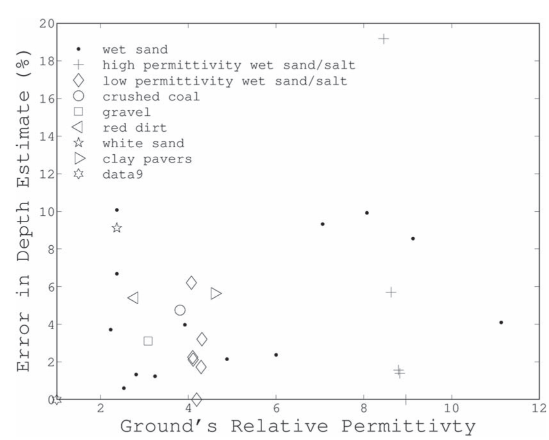

Fig. 16. Percent error in the reflector depth estimation versus the ground-truth soil permittivity: the case of the GSSI 2.6-GHz radar.

0.43, which is a very lossy material into which little or no penetration can be expected, thus making the accurate permittivity measurement redundant for most applications. To further demonstrate this, Fig. 17 shows that the return from the tub's bottom is clearly detectable for the low-loss zero-salt-content case but undetectable in the high-loss highly salty case. This is despite the material only being 10 cm thick (note that this return

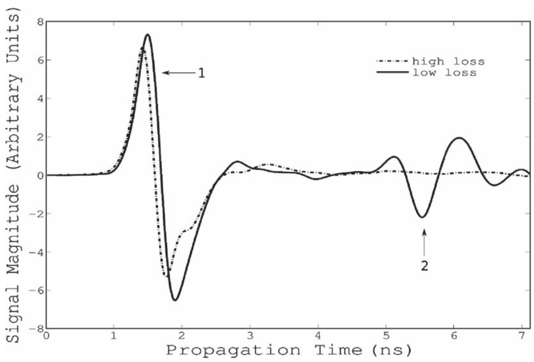

Fig. 17. A-scans from the high-permittivity variable-loss tests. Low-loss (no salt) case ground-truth $\varepsilon_r' = 8.9$, $T = 0.09$ and high-loss case ground-truth $\varepsilon_r' = 8.5$, $T = 0.43$. 1: crosstalks; 2: the return from the bottom of the tub at 10 cm only visible in the low-loss case.

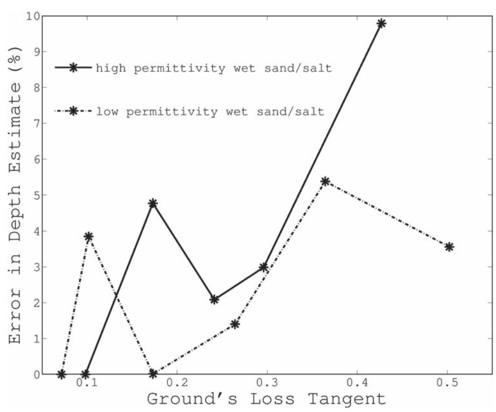

Fig. 18. Percent error in the reflector depth estimation versus the ground's loss tangent using the GSSI 1.6-GHz radar. Two tests with salt progressively added to wet sand, with the low-permittivity mix having $\varepsilon_r' \approx 4.2$ and the high-permittivity mix having $\varepsilon_r' \approx 8.7$.

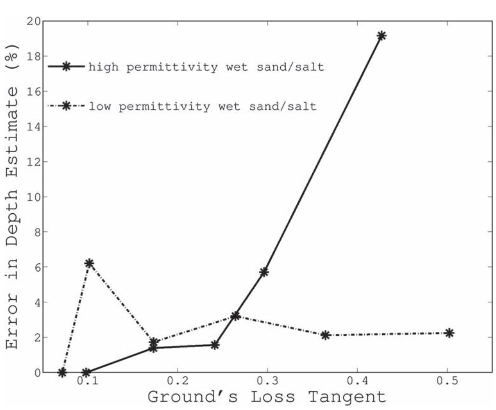

Fig. 19. Percent error in the reflector depth estimation versus the ground's loss tangent using the GSSI 2.6-GHz radar. Two tests with salt progressively added to wet sand, with the low-permittivity mix having $\varepsilon_r' \approx 4.2$ and the high-permittivity mix having $\varepsilon_r' \approx 8.7$.

remained undetected at $T = 0.30$ and was only just visibly detectable at $T = 0.24$). The two tests with constant sand/water mixtures and progressively increasing salt content were performed to further demonstrate that the proposed technique is resistant to significant variations in the ground's conductive loss. To this end, Figs. 18 and 19 plot the depth estimate error obtained for the two different radars with two different constant water/sand mixtures (constant ε_r') against the loss tangent T values obtained by increasing the salt content. These figures show that, except for one measurement at an unreasonably high loss (discussed earlier), the technique did not possess any errors above 10%. Indeed, if one considers $T = 0.3$ as the highest loss at which reasonable penetration may be obtained, then the largest error was only 6%.

V. Discussion

Although it is not the author's intended application, this technique could be used for the popular agricultural problem of soil moisture content estimation. All ground-truth permittivity values in this paper monotonically increased with respect to the moisture content, and an accurate permittivity estimation was achieved for all moisture contents tested. However, in the case of soil moisture estimation, ground penetration is not required; thus, it is important to note that the proposed technique may suffer from more significant errors when applied to highly lossy soils.

This paper has assumed the ground's permittivity to be constant across the frequency range of the GPR. Issues may occur when this assumption no longer holds. This will rarely provide a problem, however, as the GPR has a limited bandwidth and is normally used on solid ground materials that possess limited dispersive qualities. Furthermore, the close proximity of the GPR transmitters and receivers ensures that the crosstalk only travels short distances through the ground medium.

The degree to which ground antenna coupling affects the crosstalk rapidly decreases with the antenna height. As such, it is important to maintain a constant antenna height (as small as possible) and flat dielectric interfaces for both the calibration and test materials.

VI. Conclusion

This paper has presented a novel method for measuring ground permittivity. The technique characterizes the ground by measuring the frequency shift within the crosstalk of ground-coupled radars. A mathematical model that links this shift to material permittivity is proposed. The model has been thoroughly verified using both simulated and experimental results, including three different commercial radars. The technique's simplicity ensures real-time operation and easy implementation. Furthermore, it may be implemented without any knowledge of the antennas or the feed system of the radar being used. This makes it applicable to research and commercial instruments alike. It has been shown to successfully measure the permittivity of materials with a wide range of losses.

References

[1] N. Diamanti, D. Redman, and A. Giannopoulos, "A study of GPR vertical crack responses in pavement using field data and numerical modeling," in *Proc. 13th Int. Conf. GPR*, 2010, pp. 1–6.

[2] U. Spagnolini, "Permittivity measurements of multilayered media with monostatic pulse radar," *IEEE Trans. Geosci. Remote Sens.*, vol. 35, no. 2, pp. 454–463, Mar. 1997.

[3] C. Kao, J. Li, Y. Wang, H. Xing, and C. Liu, "Measurement of layer thickness and permittivity using a new multilayer model from GPR data," *IEEE Trans. Geosci. Remote Sens.*, vol. 45, no. 8, pp. 2463–2470, Aug. 2007.

[4] A. Loizos and C. Plati, "Accuracy of ground penetrating radar horn-antenna technique for sensing pavement subsurface," *IEEE Sens. J.*, vol. 7, no. 5, pp. 842–850, May 2007.
[5] L. van Kempen, H. D. Nho, H. Sahli, G. Hislop, and T. Tang, "A comparison of GPR reconstruction techniques," in *Proc. 10th Int. Conf. GPR*, 2004, vol. 1, pp. 345–348.
[6] C.-C. Chen and L. Peters, "Buried unexploded ordnance identification via complex natural resonances," *IEEE Trans. Antennas Propag.*, vol. 45, no. 11, pp. 1645–1654, Nov. 1997.
[7] T. Montoya and G. Smith, "Land mine detection using a ground-penetrating radar based on resistively loaded Vee dipoles," *IEEE Trans. Antennas Propag.*, vol. 47, no. 12, pp. 1795–1806, Dec. 1999.
[8] I. Morrow and P. Van Genderen, "Effective imaging of buried dielectric objects," *IEEE Trans. Geosci. Remote Sens.*, vol. 40, no. 4, pp. 943–949, Apr. 2002.
[9] I. Morrow, "Multi-perspective landmine detection with ground penetrating radar and the hidden Markov model," in *Proc. 8th EUCAP*, Hague, The Netherlands, Apr. 2014, pp. 3370–3371.
[10] C.-C. Chen, S. Nag, W. Burnside, J. Halman, K. Shubert, and L. Peters, "A standoff, focused-beam land mine radar," *IEEE Trans. Geosci. Remote Sens.*, vol. 38, no. 1, pp. 507–514, Jan 2000.
[11] C.-C. Chen, M. Higgins, K. O'Neill, and R. Detsch, "Ultrawide-bandwidth fully-polarimetric ground penetrating radar classification of subsurface unexploded ordnance," *IEEE Trans. Geosci. Remote Sens.*, vol. 39, no. 6, pp. 1221–1230, Jun. 2001.
[12] G. Hislop *et al.*, "Microwave radar for detection of resin defects in Pinus elliottii Engelm var elliottii," *Holzforschung*, vol. 63, no. 5, pp. 571–574, Jun. 2009.
[13] G. Hans, D. Redman, B. Leblon, J. Nader, and A. La Rocque, "Determination of log moisture content using early-time ground penetrating radar signal," *Wood Mater. Sci. Eng.*, pp. 1–18, 2014.
[14] W. Yang and S. Wang, "Coal-rock interface sensing technology applied for horizon control of mining shearers," in *Proc. ICECE*, Jun. 2010, pp. 587–590.
[15] A. D. Strange, J. C. Ralston, and V. Chandran, "Near-surface interface detection for coal mining applications using bispectral features and GPR," *Sens. Imag.: Int. J.*, vol. 6, no. 2, pp. 125–149, Apr. 2005.
[16] G. Hislop, "Measuring the thickness, permittivity and conductivity of layered earth," in *Proc. 8th EUCAP*, Apr. 2014, pp. 4367–4370.
[17] A. Kalogeropoulos, J. van der Kruk, J. Hugenschmidt, J. Bikowski, and E. Bruhwiler, "Full-waveform GPR inversion to assess chloride gradients in concrete," *NDT & E Int.*, vol. 57, pp. 74–84, Jul. 2013.
[18] A. Brancaccio, R. Pierri, G. Leone, and F. Soldovieri, "Measurements and material characterization for masonry imaging," in *Proc. 10th Int. Conf. GPR*, 2004, vol. 1, pp. 383–386.
[19] F. Soldovieri, R. Solimene, A. Brancaccio, and R. Pierri, "Localization of the interfaces of a slab hidden behind a wall," *IEEE Trans. Geosci. Remote Sens.*, vol. 45, no. 8, pp. 2471–2482, Aug. 2007.
[20] F. Soldovieri and R. Persico, "Reconstruction of an embedded slab from multifrequency scattered field data under the distorted Born approximation," *IEEE Trans. Antennas Propag.*, vol. 52, no. 9, pp. 2348–2356, Sep. 2004.
[21] G. Valerio *et al.*, "Shape reconstruction of scatterers by suitable inverse processing of GPR data," in *Proc. 6th EUCAP*, Mar. 2012, pp. 2209–2211.
[22] G. Valerio *et al.*, "GPR reconstruction of the features of Martian subsoil in the frame of the ExoMars mission," in *Proc. 5th EUCAP*, Apr. 2011, pp. 2615–2617.
[23] C. Le Bastard, V. Baltazart, Y. Wang, and J. Saillard, "Thin-pavement thickness estimation using GPR with high-resolution and superresolution methods," *IEEE Trans. Geosci. Remote Sens.*, vol. 45, no. 8, pp. 2511–2519, Aug. 2007.
[24] G. Hislop, N. Sakar, and C. Craeye, "Direction finding with MUSIC and CLEAN," *IEEE Trans. Antennas Propag.*, vol. 61, no. 7, pp. 3839–3849, Jul. 2013.
[25] E. Fisher, G. A. McMechan, and A. P. Annan, "Acquisition and processing of wide-aperture ground-penetrating radar data," *Geophys.*, vol. 57, no. 3, pp. 495–504, 1992.
[26] H. Liu, K. Takahashi, and M. Sato, "Measurement of dielectric permittivity and thickness of snow and ice on a brackish lagoon using GPR," *IEEE J. Sel. Topics Appl. Earth Observ. Remote Sens.*, vol. 7, no. 3, pp. 820–827, Mar. 2014.
[27] W. Al-Nuaimy *et al.*, "Automatic detection of buried utilities and solid objects with GPR using neural networks and pattern recognition," *J. Appl. Geophys.*, vol. 43, no. 2?4, pp. 157–165, Mar. 2000.
[28] L. Ting-jun and Z. Zheng-ou, "Fast extraction of hyperbolic signatures in GPR," in *Proc. ICMMT*, Apr. 2007, pp. 1–3.
[29] F. Soldovieri, G. Prisco, and R. Persico, "Determination of soil permittivity from GPR data and a microwave tomography approach: A preliminary study," in *Proc. 4th Int. Workshop Adv. Ground Penetrating Radar*, Jun. 2007, pp. 96–100.
[30] S. Lambot and F. Andre, "Full-wave modeling of near-field radar data for planar layered media reconstruction," *IEEE Trans. Geosci. Remote Sens.*, vol. 52, no. 5, pp. 2295–2303, May 2014.
[31] G. Hislop, S. Lambot, C. Craeye, D. Gonzalez-Ovejero, and R. Sarkis, "Antenna calibration for near-field problems with the method of moments," in *Proc. 5th EUCAP*, Apr. 2011, pp. 2004–2008.
[32] C. Warren and A. Giannopoulos, "Creating finite-difference time-domain models of commercial ground-penetrating radar antennas using Taguchi's optimization method," *Geophysics*, vol. 76, no. 2, pp. G37–G47, 2011.
[33] L. Gurel and U. Oguz, "Simulations of ground-penetrating radars over lossy and heterogeneous grounds," *IEEE Trans. Geosci. Remote Sens.*, vol. 39, no. 6, pp. 1190–1197, Jun. 2001.
[34] M. Chen and C.-C. Chen, "UWB in situ soil permittivity probe with a novel iterative permittivity calibration method," in *Proc. 14th Int. Conf. GPR*, Jun. 2012, pp. 98–102.
[35] A. Di Matteo, E. Pettinelli, and E. Slob, "Early-time GPR signal attributes to estimate soil dielectric permittivity: A theoretical study," *IEEE Trans. Geosci. Remote Sens.*, vol. 51, no. 3, pp. 1643–1654, Mar. 2013.
[36] C. Ferrara, P. Barone, C. M. Steelman, E. Pettinelli, and A. Endres, "Monitoring shallow soil water content under natural field conditions using the early-time GPR signal technique," *Vadose Zone J.*, vol. 12, no. 4, 2013.
[37] E. Pettinelli *et al.*, "Correlation between near-surface electromagnetic soil parameters and early-time GPR signals: An experimental study," *Geophys.*, vol. 72, no. 2, pp. A25–A28, 2007.
[38] E. Pettinelli *et al.*, "A controlled experiment to investigate the correlation between early-time signal attributes of ground-coupled radar and soil dielectric properties," *J. Appl. Geophys.*, vol. 101, pp. 68–76, Feb. 2014.
[39] D. Comite *et al.*, "Numerical and experimental surveys on the GPR early-time signal features for the evaluation of shallow-soil permittivity," in *Proc. 15th Int. Conf. GPR*, 2014, pp. 131–134.
[40] G. Hislop, "Ground permittivity estimation using radar to ground coupling," in *Proc. 9th EUCAP*, Apr. 2015.
[41] L. F. Chen, C. Ong, C. Neo, V. Varadan, and V. K. Varadan, *Microwave Electronics: Measurement and Materials Characterization*. New York, NY, USA: Wiley, 2004.

Greg Hislop (M'07–SM'14) was born in Australia in 1978. He received the Bachelor's degree in electrical and electronic engineering and the Ph.D. degree in inverse scattering techniques for the imaging of shallowly buried objects with ground penetrating radar from Queensland University of Technology, Brisbane, Australia, in 2000 and 2006, respectively.

From 2005 to 2008, he worked with the ICT Centre, Commonwealth Scientific and Industrial Research Organisation (CSIRO), Sydney, Australia, where he worked on the application of phase retrieval techniques to terahertz imaging applications and the detection of faults in the trunks of plantation pines using radar. From 2009 to August 2012, he worked on the direction of arrival finding techniques, novel permittivity measurement methods, and integral equation electromagnetic simulation algorithms with the Université Catholique de Louvain, Louvain-la-Neuve, Belgium. He is currently working with Energy Flagship, CSIRO, Brisbane, Australia, where he is focusing on ground penetrating radar and electromagnetic inverse scattering/sensing techniques for application to intelligent mining.

Dr. Hislop is the Chair of the IEEE Queensland Antennas and Propagation and Microwave Theory and Techniques Joint Chapter.